



High tropospheric ozone in Lhasa within the Asian summer monsoon anticyclone 2013: influence of convective transport and stratospheric intrusions

Dan Li^{1,2}, Bärbel Vogel¹, Rolf Müller¹, Jianchun Bian^{2,3}, Gebhard Günther¹, Qian Li², Jinqiang Zhang^{2,3}, Zhixuan Bai², Holger Vömel⁴, and Martin Riese¹

¹Institute of Energy and Climate Research: Stratosphere (IEK-7), Forschungszentrum Jülich, Jülich, Germany

²Key Laboratory of Middle Atmosphere and Global Environment Observation (LAGEO), Institute of Atmospheric Physics, Chinese Academy of Sciences, Beijing, China

³College of Earth Science, University of Chinese Academy of Sciences, Beijing, China

⁴Earth Observing Laboratory, National Center for Atmospheric Research, Boulder, CO, USA

Correspondence: Dan Li (da.li@fz-juelich.de) and Jianchun Bian (bjc@mail.iap.ac.cn)

Abstract. Balloon-borne measurements of ozone in Lhasa (29.66° N, 91.14° E, 3650 m above sea level) in August 2013 are investigated using backward trajectory calculations performed with the Chemical Lagrangian Model of the Stratosphere (CLaMS). Measurements show three time periods characterized by high ozone mixing ratios in the troposphere on 8, 11, and 18–20 August 2013 during the Asian summer monsoon season. Here, we could verify two different sources for the enhanced
5 ozone values in the troposphere. First, transport of polluted air from the boundary layer, and second downward transport from the stratosphere by stratospheric intrusions. Air pollution from South Asia through convective and long-range transport plays a key role in enhancing middle/upper tropospheric ozone mixing ratios up to 90% on 8 August and up to 125% on 11 August 2013. Stratospheric air intruded from the northern high-latitude to the southeastern flank of the Asian summer monsoon (ASM) anticyclone to the troposphere and is identified as source of enhanced ozone according to backward trajectory calculation and
10 satellite measurements by the Ozone Monitoring Instrument (OMI) and the Atmospheric Infrared Sounder (AIRS). Air parcels with high ozone moved from the high latitude lower stratosphere to the middle/upper troposphere and are then transported to Lhasa over a long-distance and enhanced upper middle/tropospheric ozone in Lhasa during 18–20 August 2013. Our findings demonstrate that the strong variability of ozone within the ASM anticyclone in the free troposphere is caused by transport from different regions of the atmosphere.

15 *Copyright statement.* TEXT

1 Introduction

In the upper troposphere, ozone acts as an important greenhouse gas and, thus, plays a major role in regional energy balance and in climate change. The variation of tropospheric ozone mixing ratios is associated with: (1) downward transport from



the stratosphere, or upward transport from the boundary layer; (2) photochemical production induced by solar radiation and other chemical reactions involving lighting products or ozone-precursors from biomass burning and anthropogenic pollution. Stratosphere–troposphere exchange is affecting atmospheric tracer concentrations in a significant way via upward transport from the troposphere to the stratosphere and vice versa (Holton et al., 1995; Stohl et al., 2003; Fadnavis et al., 2010; Hoor et al., 2010; Gettelman et al., 2011; Pan et al., 2016). Stratospheric intrusions transport ozone-rich air downward into the troposphere (Eisele et al., 1999; Vogel et al., 2011; Weigel et al., 2012; Langford et al., 2015). Enhanced tropospheric ozone has an impact on radiative forcing of climate (Stevenson et al., 2013).

The Asian summer monsoon (ASM) anticyclone is the most intense circulation pattern in the Northern Hemisphere in the upper troposphere and lower stratosphere (UTLS) during boreal summer (Mason and Anderson, 1963) which is forced by deep convection over South Asia (Hoskins and Rodwell, 1995). Intense monsoon convection can transport tropospheric tracers (such as hydrogen cyanide (HCN) produced by biomass burning, carbon monoxide (CO), nitrogen oxides (NO_x) or aerosols) from the lower troposphere into the UTLS of the ASM anticyclone or its edge (Chen et al., 2012; Vogel et al., 2015; Tissier and Legras, 2016; Li et al., 2017; Fan et al., 2017b). Because of the strong dynamical confinement of the ASM anticyclone in the UTLS region in summer (Ploeger et al., 2015; Pan et al., 2016; Vogel et al., 2016), tropospheric tracer gases show a local maximum near the tropopause layer within the ASM anticyclone according to satellite measurements (e.g. Park et al., 2009; Randel et al., 2010; Vernier et al., 2015; Yan and Bian, 2015; Yu et al., 2017). At the edge of the ASM anticyclone, tropospheric tracers within the ASM anticyclone are transported outside, will affect trace gas concentrations in the UTLS result in significant changes in radiative forcings.

The ASM anticyclone is also an active region for stratosphere–troposphere exchange (e.g. Škerlak et al., 2014; Garny and Randel, 2016; Fan et al., 2017a). In-situ balloon measurements in August 2015 in Kunming, China combined with satellite data and model simulations show that anthropogenic emissions from Asia play a significant role in the tropopause aerosol layer formation within the ASM anticyclone (Yu et al., 2017). Vogel et al. (2016) show that the northeastern flank of the ASM anticyclone is a region where air masses from the ASM anticyclone are separated from the anticyclone and are subsequently transported into the extra-tropical lower stratosphere. When air parcels enter into the stratosphere, they have the potential to impact the regional climate in Asia (Vernier et al., 2015; Gu et al., 2016). Furthermore, stratospheric intrusions occur at the northeastern flank of the anticyclone and transport dry ozone-rich air into the troposphere over northern India. Stratospheric intrusions or tropopause folds have the potential to influence surface weather (e.g. monsoon deficit rainfall, Fadnavis and Chattopadhyay, 2017).

Balloon-borne measurements provided highly accurate water vapour and ozone profiles. Measurements with such balloon payloads have been carried out since 2009 in Lhasa and Kunming (Bian et al., 2012; Li et al., 2017), in Nainital (Brunamonti et al., 2018), and in southern India and South America (Vernier et al., 2018). Low ozone values measured in the upper troposphere in Lhasa were present by Li et al. (2017), rapid vertical transport associated with typhoon convection lead to this phenomenon. The ozone profile in Li et al. (2017) also shows anomalies of high ozone values in the middle/upper troposphere over the Tibetan Plateau, however, they gave limited explanation about this phenomenon. It is important to investigate the ozone variation over the Tibet Plateau, in order to quantify the uncertainty of the radiative forcing from tropospheric ozone in



climate model. In this study, we combined these in-situ measurements with satellite data and trajectory calculations using the Chemical Lagrangian Model of the Stratosphere (CLaMS) model (McKenna et al., 2002; Pommrich et al., 2014) to analyse the high ozone structure found in the middle/upper troposphere in Lhasa over the Tibetan Plateau in August 2013. This paper is organized as follows: Sect. 2 describes the balloon sonde data, satellite data, and the CLaMS model. In Sect. 3, we present three case studies with enhanced tropospheric ozone in August 2013. A summary is given in the final section.

2 Measurements and trajectory calculations

2.1 Balloon-borne measurements

Vertical profiles of ozone and water vapour shown in this study are from the SWOP campaign in August 2013. A total of 24 balloons were launched during nighttime between 22:00 BST (Beijing Standard Time, UTC+8) and 23:00 BST in Lhasa. The payload consists of an electrochemical concentration cell (ECC) ozonesonde (Komhyr et al., 1995) to measure ozone, a cryogenic frost point hygrometer (CFH) (Vömel et al., 2007, 2016) to measure the frost (dew) point temperature for the temperature below (above) -15°C , and a compact optical backscatter aerosol detector (COBALD, developed at the Swiss Federal Institute of Technology, Zürich) backscatter sonde to detect aerosol or ice cloud backscatter (Brabec et al., 2012). An iMet radiosonde was used to transmit the CFH and Cobald data as well as to measure the ambient temperature, pressure, relative humidity (RH), and wind speed/direction. Further details about the different balloon flights during the SWOP campaign in 2013 are given by Li et al. (2017).

The relative humidity over ice (RH_i) from CFH is defined as

$$\text{RH}_i = \frac{e}{e_{sat}} \times 100\% \quad (1)$$

where e is the water vapour pressure calculated from the frost point or dew point temperature and e_{sat} is the saturated vapour pressure with respect to liquid water or ice, which is calculated from the ambient temperature using the Hyland–Wexler equation (Hyland and Wexler, 1983) for liquid water and Goff–Gratch equation (Goff and Gratch, 1946) for ice water. The RH_i uncertainty is 5% in the tropopause layer (Vömel et al., 2016).

The colour index (CI) (Rosen and Kjome, 1991) is defined as

$$\text{Colour index} = \frac{\text{BSRred} - 1}{\text{BSRblue} - 1} \quad (2)$$

where BSRblue and BSRred are backscatter ratios at wavelengths of 455 nm and 940 nm, respectively. CI is used to separate in-cloud ($\text{CI} > 7$) from clear sky ($\text{CI} < 7$) (Vernier et al., 2015; Brunamonti et al., 2018).

2.2 Satellite data

The ozone monitoring instrument (OMI) is a nadir viewing near ultraviolet/visible charge–coupled spectrometer aboard the National Aeronautics and Space Administration’s (NASA’s) Earth observing system’s Aura satellite (Levelt et al., 2006). In



this study we use the TOMS–Like total column ozone level-3 product (OMTO3e) with horizontal resolution 0.25×0.25 . The TOMS version 8 algorithm is used to extract the vertical column ozone data using only two wavelengths (317.5 and 331.2 nm). The strong ozone absorption at 317.5 nm is used to derive total ozone, and the weaker absorb at 331.2 nm is used to estimate the effective surface reflectivity. The relative uncertainty on OMI-TOMS product is less than 5%.

5 The atmospheric infrared sounder (AIRS) on NASA's Aqua satellite is on a sun synchronous polar orbit. The instrument employs a cross-track scanning hyper-spectral infrared spectrometer with 2378 spectral channels (Aumann et al., 2003). It is designed to provide twice daily global data sets for different constituents and temperature. Here we use the AIRS Level-2 ozone and water retrieval product version 6.0 (Olsen et al., 2013).

CloudSat is designed to probe the vertical structure of clouds and precipitation using a cloud profiling radar (CPR), as
10 a component of the A-Train (Marchand et al., 2008). The Cloudsat operational 2B Geometric Profile (2B-GEOPROF) data product (Version R04) is used with 480 m vertical resolution. The vertical distribution of radar reflectivity is used to mark cloud layer. The echo mask values are greater than 20 dBZe indicating a false detection value below 16%.

2.3 Model

Fifty-day backward trajectories are started along the ascent profile of each balloon flight in Lhasa in August 2013. The diabatic
15 trajectories are calculated using the CLaMS trajectory model (McKenna et al., 2002; Konopka et al., 2004; Pommrich et al., 2014). The trajectories of air parcels are calculated using the classical fourth-order Runge–Kutta method with a 1800-second time step. The CLaMS model employs a hybrid pressure-potential temperature coordinate, detail information about the vertical coordinate was presented by Konopka et al. (2007). The trajectory has been used to focus on the transport process within or around the ASM anticyclone (Vogel et al., 2015, 2018; Ploeger et al., 2015). Dynamic fields from the European Centre for
20 Medium-range Weather Forecasts (ECMWF) interim reanalysis (Era-Interim) (Dee et al., 2011) are used to drive the CLaMS model. The input dynamic fields are recorded every 6 hours on a $1^\circ \times 1^\circ$ horizontal grid with 60 hybrid vertical levels from the surface to 0.1 hPa. The vertical velocity on hybrid level is calculated using the diabatic heating budget including the cloud radiation, latent heat release, and mixing and diffusion (Ploeger et al., 2010). The trajectory model setup is the same as in Li et al. (2017).

25 3 Results and Discussion

The ozone profiles over Lhasa show a pronounced daily variation of ozone mixing ratios (OMR) between 340 K and 430 K from 4 to 27 August 2013 (Fig. 1). The lapse-rate tropopause is calculated from measured temperature profiles using the lapse-rate criteria of the World Meteorological Organization (WMO) definition (WMO, 1957). The lapse rate tropopause in Lhasa range from 365 K to 410 K in August 2013. Low ozone values were measured in the upper troposphere on 11, 19, and 24 August
30 2013 (Fig. 1). Li et al. (2017) have combined balloon-borne measurements with CLaMS trajectory model to highlight the low ozone structures in the upper troposphere over Lhasa. A major reason why ozone mixing ratios in the upper troposphere remain low is the impact from tropical cyclones, which transport marine boundary layer air with low ozone to the upper troposphere



over Lhasa. However, two profiles with extreme high ozone mixing ratios, up to 180 ppbv are found at upper troposphere (355–365 K) on 8 August and in the troposphere from 330 K to 352 K on 11 August 2013 (Fig. 1). Further, episodes with high ozone mixing ratios occurred from the middle troposphere to the lower stratosphere during 18–20 August 2013. Whereas Li et al. (2017) discuss low ozone values in August 2013, here we will focus on extreme high ozone values.

5 3.1 High ozone and long-range transport on 8 August 2013

Figure 2a shows the vertical profiles of temperature, OMR, monthly mean ozone, RH, and OMR relative change. The positive OMR anomalies with value up to 180 ppbv occur between 355 K and 365 K, which is below the lapse rate tropopause (378 K) at 22:41 BST on 8 August 2013 (Fig. 2a left). The OMR relative change shown in Fig. 2a (right) shows the percentage deviation of the ozone profile observed on 8 August from the monthly mean ozone profile obtained by averaging 24 profiles over Lhasa in August 2013. The data shows ozone anomalies up to 90 % on August 8. The high ozone value is marked by dark shade for the OMR relative changes above 30%; in the following, we solely focus on these air masses. Unfortunately, RH_i from CFH are not available above 335 K. Instead, the relative humidity (RH) from iMet was used, with useful data just below 350 K (above -40°C). Below -40°C , RH will not be used, because of the detection limit of the radiosonde humidity sensor.

The potential vorticity (PV) along the 30-day backward trajectories of air parcels within high ozone layer between 355 K and 363 K was shown in Fig. 2b as a function of time and potential temperature. According to their different pathways, backward trajectories of air parcels could be divided into two clusters. Both of them experienced strong uplift processes with potential temperature increasing from 330 K to 360 K on 20 and 29 July. The tracks of 20-day backward trajectories of air parcels around 355–363 K isentropes initialized on 8 August 2013 are shown colour-coded by date in Fig. 2c. Air parcels started their ascent near the Himalayas and were uplifted to 360 K isentrope between 19 and 21 July and then moved horizontally to East Asia following the ASM anticyclone. Finally, the air parcels moved westerly around the anticyclone circulation before they arrived in Lhasa on 8 August 2013. The transport time for the air parcels from the lower troposphere of the Himalayas to the upper troposphere over Lhasa is less than 20 days for the whole pathway.

Figure 2d gives the boundary layer geolocation of air parcels (the same as in Fig. 2b and c), where they experience strong uplift through convection. The uplift rate of air parcel is defined as $(\theta_{t+\delta t} - \theta_{\delta t})/\delta t$. When the uplift rate is greater than 9 K day^{-1} (an empirical value), the strong uplift process of air parcels will be recognized. The point that air parcels start ascent is marked as the geolocation. We find that most of air parcels were from the Himalayas, where strong uplift occurred frequently. South Asia, the area adjacent to the Himalayas is usually a strong source region of air pollution, which is caused by natural (e.g. biomass burning) and anthropogenic processes (Cong et al., 2015). In addition, ozone is photochemically enhanced by reactions involving ozone precursors from biomass burning. After reaching the upper troposphere, the polluted air masses that were transported over long distances, made the best possible contribution to high tropospheric ozone over Lhasa at nighttime on 8 August 2013.



3.2 High ozone and high water vapour on 11 August 2013

The vertical variability of OMR, monthly mean ozone, temperature, the OMR relative change, RH_i , and colour index on 11 August 2013 is shown in Fig. 3a. Positive ozone anomalies (Fig. 3a left) and the OMR positive variance (Fig. 3a right) appeared from the surface to the mid-troposphere (330–353 K) at 22:40 BST on 11 August 2013. The RH_i shows high value (>70%) between 336 K and 350 K. Colour index from the COBALD shows that a thick cirrus cloud layer occurred below 349 K. The finding of high ozone mixing ratios accompanied by high water vapour values within a thick cloud layer is not consistent with previous studies. The ozone mixing ratio is usual low within cloud. Due to the detection limit for chemical composition over the Tibetan Plateau during this period, it is different to describe what takes place when pollution air met the cirrus cloud.

PV values along the 50-day backward trajectories of air parcels within high ozone mixing ratios between 340 K and 354 K are shown in Fig. 3b. The results show that the PV values are less than 1.5 PVU in the troposphere. Air parcels were uplifted to the upper troposphere through convection, then they are transported over a long distance and descended before they arrived in Lhasa. 3-dimensional backward trajectories of air parcels within the high ozone structure were shown in Fig. 3c. Particles were first uplifted to the upper troposphere and these were moved around the ASM anticyclone within 4–5 weeks. Vogel et al. (2014) demonstrate that it is possible for air parcels from the western Pacific boundary layer to impact the chemical composition in the stratosphere over northern Europe within 5 weeks based on the CLaMS trajectory calculations. Polluted air from South Asia boundary layer has the potential to impact the ozone structure over Lhasa via transportation within 4–5 weeks.

Fig. 3d gives the boundary layer geolocation, where parcels experienced strong uplift. Most of the air parcels are transported from South/Southeast Asia, a region with high air pollution. Few of the air parcels originated from South China and the Tibetan Plateau. Obviously, the RH_i is controlled by local microphysical cloud processes according to the colour index ($CI > 7$, in-cloud). The horizontal scale of the cloud is less than 1×1 degree according to the MODIS satellite (figure not shown). Air pollutants from South Asia or Lhasa may contribute to the positive ozone anomalies over Lhasa through photochemical production, however, due to the detection limit for chemical constituents that produces ozone, we can not answer this question conclusively.

3.3 Stratospheric intrusion on 18–20 August 2013

Figure 4 shows the total column ozone (TCO) from the OMI satellite along with the geopotential height, PV at 150 hPa, and the sea-level pressure of typhoon Utor on 16 August 2013. The PV clearly displays a filament structure extending from northeastern Asia to the southeastern edge of the ASM anticyclone on 16 August 2013 (Fig. 4a). TCO displays the same structure as the PV over northeastern Asia, where stratospheric intrusions occur frequently (Li and Bian, 2015; Song et al., 2016). The enhanced TCO values are first of all indicative for an extra-tropical intrusion. Since the stratosphere contributes most to the column, it is also indicative for an intrusion of stratospheric air. This is further supported by the good correlation of TCO with PV values at 150 hPa. The filament structure is subsequently separated from the stratosphere. The remnant of the stratospheric intrusion (Rossby wave breaking filament) moves westward along the easterly wind flow at the southern flank of the ASM anticyclone. During the next days, this broken filament structure moves westward about 3,000 km. It arrives in Lhasa and is captured by



the ozonesondes launched on 18, 19, and 20 August 2013 (Fig. 4b–d), contributing to the positive ozone value measured in the UTLS region over Lhasa (the black rectangles in Fig. 1). The stratospheric intrusion with high ozone mixing ratios is also reflected in low water vapour values observed by AIRS at 346 hPa during its ascending track on 16 August 2013 (Fig. 4e and 4f).

5 Figure 5a shows the vertical variability of ozone, monthly mean ozone, temperature, RH_i , colour index, and the OMR relative change for 18 August 2013. The positive OMR relative change appears in the troposphere around 350 K and 363–373 K, and the lower stratosphere (Fig. 5a right). Two characteristic minima of OMR relative change occur between 352–357 K and 375–390 K on 18 August. RH_i is anti-correlated with OMR anomalies on these isentropic surfaces. RH_i near the tropopause (384 K) is greater than 100%. Indeed, an ice cloud layer was observed near the tropopause layer according to the colour index
10 (CI>7) from COBALD backscatter measurements. Super-saturation is observed within the ice cloud.

In order to investigate in detail the variance of ozone profiles measured on 18 August 2013, the PV along the 50-day backward trajectories from the CLaMS model is displayed in Figure 5b. Parcels in the upper troposphere (363–373 K) originate from the dry intrusion layer. There is evidence for mixing processes that occurred between air parcels with high PV from stratosphere and low PV value from the troposphere, while air parcels in the middle troposphere (around 350 K) with high ozone and
15 low water vapour originate from the thin intrusion layer. Air parcels around 350 K experienced a weak uplift during 13–14 August 2013. Figure 5c shows the tracks of backward trajectories of air parcels on 350–352 K and 363–373 K on 18 August, respectively. Only 15-day backward trajectories of air parcels are shown colour-coded with potential temperature here. This is long enough to show the intrusion pathway. The thin intrusion layer with low potential temperature (338 K) moved toward the north around the anticyclone and then shows a strong equatorward movement from 60° N to 30° N around 60° E. The
20 intrusion layer in the upper troposphere experienced mixing process according to the PV along the trajectories. Air parcels with high PV values from the Northern Hemisphere were mixed with air parcels with low PV from the equatorial region at approximately 35° N, 60° W over the North Atlantic. Although ozone-rich air mixed with ozone-poor air from the equatorial region, the positive ozone anomalies still appeared in the upper troposphere on 18 August 2013.

Positive ozone mixing ratio anomalies were also captured on 19 and 20 August 2013. The variability of ozone vertical structure is significant in the middle troposphere on 19 August. Ozone and water vapour show strong anti-correlation below 355 K. The OMR relative change shows large increase in the tropopause region (368–408 K), up to 90% (Fig. 6a). The 50-day backward trajectories of air parcels in Fig. 6b indicate diabatic decent transport process, especially the air cluster in the middle troposphere (between 347 K and 355 K). The PV along the trajectories of air parcels between 368 K and 380 K display high PV with values greater than 6 PVU. Figure 6c shows the tracks of backward trajectories of air parcels within high ozone in
30 the middle and upper troposphere on 19 August. The stratospheric intrusion in the middle troposphere has the same transport pathway as on 18 August and also experienced an uplift process around 14 August. Air parcels near the tropopause layer (Fig. 6a) originated from the northern Hemisphere with high ozone and high PV. The equatorial regions contribute little to air parcels on 19 August compared to the case on 18 August. That is why the OMR relative change near the tropopause layer on 19 August is higher than OMR relative change on 18 August.



The ozone vertical structure and RH_i also show an anti-correlation in the middle troposphere on 20 August. In the troposphere, the OMR relative change near 355 K is higher than 30%. The OMR relative change on 20 August shows minor increases in the tropopause region (Fig. 7a) and is also weaker than on 19 August. The lapse rate tropopause height on 20 August is lower than on 18 and 19 August. Fig. 7b shows the PV along the backward trajectories of air parcels in the middle troposphere (355 K) on 20 August. The intrusion in the middle troposphere has the same transport pathway as the one on 18 August and also experienced an uplift process around 14 August (Fig. 7c).

Figure 8a–c show the cross section of the square of the Brunt–Vaisala frequency (N^2) along the average longitude of the bottom air cluster in Fig. 5b on 10 August at 06:00 UTC, on 12 August at 18:00 UTC, and on 13 August at 12:00 UTC with potential temperature, PV, zonal wind, and the lapse rate tropopause calculated from the ERA-Interim reanalysis. The radar reflectivities measured by the CloudSat's CPR are shown in Fig. 8d. Air parcels are located in the extra-tropical lowermost stratosphere (350–380 K) above the lapse rate tropopause (near 330 K) on 10 August 2013 at 06:00 UTC (Fig. 8a). These parcels moved equatorward and arrived at the poleward edge of westerly wind jet two days later, where a tropopause folding occurred (Fig. 8b). Parcels continue to move along the isentropic surfaces and cross the tropopause region from the polar lowermost stratosphere to the upper troposphere in the mid-latitude on 13 August 2013 at 12:00 UTC (Fig. 8c). Overall, it takes 2–3 days for air parcels to cross the tropopause. Both the pathway and timescale of transport are consistent with the analysis of other deep stratospheric intrusions that occurred over North America (Langford et al., 1996; Vogel et al., 2011; Kuang et al., 2012; Lin et al., 2015) or Europe (Stohl and Trickl, 1999; Trickl et al., 2010, 2014) associated with the polar jet stream. It is interesting that in our case, air parcels are affected by strong convection in the troposphere, after they are transported from the stratosphere downward into the upper troposphere. The strong convection lifted air parcels to high altitude, which can be seen from the CloudSat radar reflectivity (dBZe) (Fig. 8d). This uplift process can be seen clearly on 14 August 2013 in Fig. 5b. The extra-tropical tropopause is located between the upper troposphere and lower stratosphere and intersects the isentropic surface, which acts as a dynamic barrier for tracer transport (Gettelman et al., 2011). Ozone in the extratropics exhibit large gradients in the UTLS. There is a net downward transport of ozone from the stratosphere to the troposphere along the isentrope at the poleward edge of the jets (Yang et al., 2016). The tropopause fold transports air parcels quasi-isentropically from the lowermost stratosphere with high ozone mixing ratio to the troposphere within the ASM anticyclone, contributing to high tropospheric ozone over Tibetan Plateau on 18, 19, and 20 August 2013.

4 Conclusions

Balloon-borne measurements of ozone and water vapour mixing ratios over Lhasa in August 2013 are investigated using the OMI and AIRS satellite data and backward trajectory calculations from the CLaMS model. We focus on enhanced ozone mixing ratios observed in the middle/upper troposphere over Lhasa on 8, 11, and 18–20 August.

For 8 and 11 August, our trajectory calculations show that the enhanced ozone mixing ratios result from air pollution from south Asia, which reached the measurement location through convective and long-range transport. According to the result of our trajectory calculations, complemented by OMI and AIRS satellite data, the ozone enhancement observed during the time



period from 18 to 20 August 2013 resulted from a stratospheric intrusion, which occurred over the southeastern edge of the ASM anticyclone. The intrusion resulted in high ozone and low water vapour values in the middle/upper troposphere over Lhasa within the ASM anticyclone, thereby highlighting the important role of large-scale atmospheric dynamic transport for the trace gas budget in this region.

5 The satellite data and the trajectory calculations from the CLaMS model indicate that both stratospheric intrusions and convective transport of air pollution play a major role in enhancing middle/upper tropospheric ozone over Lhasa, China. However, the PV along the backward trajectories for the convective transport and the stratospheric intrusion are different. The PV values along the trajectories are less than 2 PVU for the convective transport case, and greater than 6 PVU for the stratospheric intrusion when air parcels are located in the extra-tropical lower stratosphere. The PV decrease when air parcel
10 cross the lapse rate tropopause from the lower stratosphere to the troposphere. Tropical cyclones, which could transport marine boundary layer air with low ozone to the upper troposphere, lead to low ozone values in the upper troposphere in August in Lhasa (Li et al., 2017). The variability of the middle/upper tropospheric ozone over Lhasa in 2013 is the result of different advective and convective transport processes transporting air from different regions to Lhasa. Studies indicate that ozone
15 concentrations in the marine boundary layer by tropical cyclones, and the polluted air in South Asia.

Data availability. ERA-Interim meteorological reanalysis data are free available from the web page: <http://apps.ecmwf.int/datasets/data/interim-full-daily/levtype=sfc/>. The OMI ozone data were download from <https://search.earthdata.nasa.gov/>. The AIRS Level-2 data used in this study can be obtained at https://airs12.gesdisc.eosdis.nasa.gov/data/Aqua_AIRS_Level2/. The CloudSat products are provided on www.cloudsat.cira.colostate.edu. The SWOP data of this paper are available upon request to Jianchun Bian (bjc@mail.iap.ac.cn). The CLaMS
20 backward trajectories calculations can be requested from Dan Li (lidan@mail.iap.ac.cn).

Competing interests. The authors declare that they have no conflict of interest

Acknowledgements. Ozone and water vapour data are from the SWOP campaign, which is funded by the National Natural Science Foundation of China (41605025, 41675040, and 91637104). Our activities contribute to the European Community's Seventh Framework Programme (FP7/2007-2013) as part of the StratoClim project (grant agreement no. 603557). This work was supported by International Postdoctoral Exchange Fellowship Program 2017 under grant no. 20171015 and China Postdoctoral Science Foundation (2015M581153).
25



References

- Aumann, H. H., Chahine, M. T., Gautier, C., Goldberg, M., Kalnay, E., McMillin, L., Revercomb, H., Rosenkranz, P. W., Smith, W. L., Staelin, D., Strow, L., and Susskind, J.: AIRS/AMSU/HSB on the Aqua Mission: Design, Science Objectives, Data Products and Processing Systems, *IEEE Trans. Geosci. Remote Sens.*, 41, 253–264, 2003.
- 5 Bian, J. C., Pan, L. L., Paulik, L., Vömel, H., and Chen, H. B.: In situ water vapor and ozone measurements in Lhasa and Kunming during the Asian summer monsoon, *Geophys. Res. Lett.*, 39, L19808, <https://doi.org/10.1029/2012GL052996>, 2012.
- Brabec, M., Wienhold, F. G., Luo, B. P., Vömel, H., Immler, F., Steiner, P., Hausammann, E., Weers, U., and Peter, T.: Particle backscatter and relative humidity measured across cirrus clouds and comparison with microphysical cirrus modelling, *Atmos. Chem. Phys.*, 12, 9135–9148, <https://doi.org/10.5194/acp-12-9135-2012>, <http://www.atmos-chem-phys.net/12/9135/2012/>, 2012.
- 10 Brunamonti, S., Jorge, T., Oelsner, P., Hanumanthu, S., Singh, B. B., Kumar, K. R., Sonbawne, S., Meier, S., Singh, D., Wienhold, F. G., Luo, B. P., Böttcher, M., Poltera, Y., Jauhainen, H., Kayastha, R., Dirksen, R., Naja, M., Rex, M., Fadnavis, S., and Peter, T.: Balloon-borne measurements of temperature, water vapor, ozone and aerosol backscatter at the southern slopes of the Himalayas during StratoClim 2016-2017, *Atmos. Chem. Phys. Discuss.*, 2018, 1–38, <https://doi.org/10.5194/acp-2018-222>, <https://www.atmos-chem-phys-discuss.net/acp-2018-222/>, 2018.
- 15 Chen, B., Xu, X. D., Yang, S., and Zhao, T. L.: Climatological perspectives of air transport from atmospheric boundary layer to tropopause layer over Asian monsoon regions during boreal summer inferred from Lagrangian approach, *Atmos. Chem. Phys.*, 12, 5827–5839, <https://doi.org/10.5194/acp-12-5827-2012>, 2012.
- Cong, Z., Kawamura, K., Kang, S., and Fu, P.: Penetration of biomass-burning emissions from South Asia through the Himalayas: new insights from atmospheric organic acids, *Sci. Rep.*, 5, 9580, <https://doi.org/10.1038/srep09580>, 2015.
- 20 Dee, D. P., Uppala, S. M., Simmons, A. J., Berrisford, P., Poli, P., Kobayashi, S., Andrae, U., Balmaseda, M. A., Balsamo, G., Bauer, P., Bechtold, P., Beljaars, A. C. M., van de Berg, L., Bidlot, J., Bormann, N., Delsol, C., Dragani, R., Fuentes, M., Geer, A. J., Haimberger, L., Healy, S. B., Hersbach, H., Hólm, E. V., Isaksen, I., Kållberg, P., Köhler, M., Matricardi, M., McNally, A. P., Monge-Sanz, B. M., Morcrette, J.-J., Park, B.-K., Peubey, C., de Rosnay, P., Tavolato, C., Thépaut, J.-N., and Vitart, F.: The ERA-Interim reanalysis: configuration and performance of the data assimilation system, *Q. J. R. Meteorol. Soc.*, 137, 553–597, <https://doi.org/10.1002/qj.828>, 2011.
- 25 Eisele, H., Scheel, H. E., Sladkovic, R., and Trickl, T.: High-resolution lidar measurements of stratosphere-troposphere exchange, *J. Atmos. Sci.*, 56, 319–330, [https://doi.org/10.1175/1520-0469\(1999\)056<0319:HRLMOS>2.0.CO;2](https://doi.org/10.1175/1520-0469(1999)056<0319:HRLMOS>2.0.CO;2), 1999.
- Fadnavis, S. and Chattopadhyay, R.: Linkages of subtropical stratospheric intraseasonal intrusions with Indian summer monsoon deficit rainfall, *J. Clim.*, 30, 5083–5095, <https://doi.org/10.1175/JCLI-D-16-0463.1>, 2017.
- Fadnavis, S., Chakraborty, T., and Beig, G.: Seasonal stratospheric intrusion of ozone in the upper troposphere over India, *Ann. Geophys.*, 28, 2149–2159, <https://doi.org/10.5194/angeo-28-2149-2010>, 2010.
- 30 Fan, Q., Bian, J., and Pan, L. L.: Stratospheric entry point for upper-tropospheric air within the Asian summer monsoon anticyclone, *Sci. China Earth Sci.*, 60, 1685–1693, <https://doi.org/10.1007/s11430-016-9073-5>, <https://doi.org/10.1007/s11430-016-9073-5>, 2017a.
- Fan, Q.-J., Bian, J.-C., and Pan, L. L.: Atmospheric boundary layer sources for upper tropospheric air over the Asian summer monsoon region, *Atmos. Oceanic Sci. Lett.*, 10, 358–363, <https://doi.org/10.1080/16742834.2017.1344089>, <https://doi.org/10.1080/16742834.2017.1344089>, 2017b.
- 35 Garny, H. and Randel, W. J.: Transport pathways from the Asian monsoon anticyclone to the stratosphere, *Atmos. Chem. Phys.*, 16, 2703–2718, <https://doi.org/10.5194/acp-16-2703-2016>, 2016.



- Gottelman, A., Hoor, P., Pan, L. L., Randel, W. J., Hegglin, M. I., and Birner, T.: The extratropical upper troposphere and lower stratosphere, *Rev. Geophys.*, 49, RG3003, <https://doi.org/10.1029/2011RG000355>, 2011.
- Goff, J. A. and Gratch, S.: Low-pressure properties of water from -160 to 212 F, *Trans. Am. Soc. Heating Air-Cond. Eng.*, 52, 95–122, 1946.
- 5 Gu, Y., Liao, H., and Bian, J.: Summertime nitrate aerosol in the upper troposphere and lower stratosphere over the Tibetan Plateau and the South Asian summer monsoon region, *Atmos. Chem. Phys.*, 16, 6641–6663, <https://doi.org/10.5194/acp-16-6641-2016>, 2016.
- Holton, J. R., Haynes, P., McIntyre, M. E., Douglass, A. R., Rood, R. B., and Pfister, L.: Stratosphere-troposphere exchange, *Rev. Geophys.*, 33, 403–439, 1995.
- Hoor, P., Wernli, H., Hegglin, M. I., and Boenisch, H.: Transport timescales and tracer properties in the extratropical UTLS, *Atmos. Chem.*
- 10 *Phys.*, 10, 7929–7944, <https://doi.org/10.5194/acp-10-7929-2010>, 2010.
- Hoskins, B. J. and Rodwell, M. J.: A model of the Asian summer monsoon. Part I: The global scale, *J. Atmos. Sci.*, 52, 1329–1340, 1995.
- Hyland, R. W. and Wexler, A.: Formulations for the thermodynamic properties of the saturated phases of H_2O from 173.15 K to 473.15 K, *ASHRAE Trans.*, 89, 500–519, 1983.
- Komhyr, W. D., Barnes, R. A., Brothers, G. B., Lathrop, J. A., and Opperman, D. P.: Electrochemical concentration cell ozonesonde performance evaluation during STOIC 1989, *J. Geophys. Res.*, 100, 9231–9244, <https://doi.org/10.1029/94JD02175>, 1995.
- 15 Konopka, P., Steinhorst, H.-M., Groß, J.-U., Günther, G., Müller, R., Elkins, J. W., Jost, H.-J., Richard, E., Schmidt, U., Toon, G., and McKenna, D. S.: Mixing and Ozone Loss in the 1999–2000 Arctic Vortex: Simulations with the 3-dimensional Chemical Lagrangian Model of the Stratosphere (CLaMS), *J. Geophys. Res.*, 109, D02315, <https://doi.org/10.1029/2003JD003792>, 2004.
- Konopka, P., Günther, G., Müller, R., dos Santos, F. H. S., Schiller, C., Ravegnani, F., Ulanovsky, A., Schlager, H., Volk, C. M., Viciani, S.,
- 20 Pan, L. L., McKenna, D.-S., and Riese, M.: Contribution of mixing to upward transport across the tropical tropopause layer (TTL), *Atmos. Chem. Phys.*, 7, 3285–3308, 2007.
- Kuang, S., Newchurch, M. J., Burris, J., Wang, L., Knupp, K., and Huang, G.: Stratosphere to troposphere transport revealed by groundbased lidar and ozonesonde at a midlatitude site, *J. Geophys. Res.*, 117, <https://doi.org/10.1029/2012JD017695>, <http://https://doi.org/10.1029/2012JD017695>, 2012.
- 25 Langford, A. O., Masters, C. D., Proffitt, M. H., Hsie, E.-Y., and Tuck, A. F.: Ozone measurements in a tropopause fold associated with a cut-off system, *Geophys. Res. Lett.*, 23, 2501–2504, <https://doi.org/10.1029/96GL02227>, 1996.
- Langford, A. O., Pierce, R. B., and Schultz, P. J.: Stratospheric intrusions, the Santa Ana winds, and wildland fires in Southern California, *Geophys. Res. Lett.*, 42, 6091–6097, <https://doi.org/10.1002/2015GL064964>, 2015.
- Levelt, P. F., Van den Oord, G. H. J., Dobber, M. R., Mälkki, A., Visser, H., de Vries, J., Stammes, P., Lundell, J. O. V., and Saari, H.: The
- 30 ozone monitoring instrument, *IEEE Trans. Geophys. Remote Sens.*, 44, 1093–1101, <https://doi.org/10.1109/TGRS.2006.872333>, 2006.
- Li, D. and Bian, J.: Observation of a Summer Tropopause Fold by Ozonesonde at Changchun, China: Comparison with Reanalysis and Model Simulation, *Adv. Atmos. Sci.*, 32, 1354–1364, <https://doi.org/10.1007/s00376-015-5022-x>, 2015.
- Li, D., Vogel, B., Bian, J., Müller, R., Pan, L. L., Günther, G., Bai, Z., Li, Q., Zhang, J., Fan, Q., and Vömel, H.: Impact of typhoons on the composition of the upper troposphere within the Asian summer monsoon anticyclone: the SWOP campaign in Lhasa 2013, *Atmos. Chem.*
- 35 *Phys.*, 17, 4657–4672, <https://doi.org/10.5194/acp-17-4657-2017>, 2017.
- Lin, M., Fiore, A. M., Horowitz, L. W., Langford, A. O., Oltmans, S. J., Tarasick, D., and Rieder, H. E.: Climate variability modulates western US ozone air quality in spring via deep stratospheric intrusions, *Nat. Commun.*, 6, 7105, <https://doi.org/10.1038/ncomms8105>, 2015.



- Marchand, R., Mace, G. G., Ackerman, T., and Stephens, G.: Hydrometeor Detection Using Cloudsat-An Earth-Orbiting 94-GHz Cloud Radar, *J. Atmos. Ocean. Technol.*, 25, 519–533, <https://doi.org/10.1175/2007JTECHA1006.1>, 2008.
- Mason, B. R. and Anderson, E. C.: The development and decay of the 100-mb. summertime anticyclone over southern Asia, *Mon. Wea. Rev.*, 91, 3–12, [https://doi.org/10.1175/1520-0493\(1963\)091<0003:TDADOT>2.3.CO;2](https://doi.org/10.1175/1520-0493(1963)091<0003:TDADOT>2.3.CO;2), 1963.
- 5 McKenna, D. S., Konopka, P., Grooß, J.-U., Günther, G., Müller, R., Spang, R., Offermann, D., and Orsolini, Y.: A new Chemical Lagrangian Model of the Stratosphere (CLaMS): 1. Formulation of advection and mixing, *J. Geophys. Res.*, 107, 4309, <https://doi.org/10.1029/2000JD000114>, 2002.
- Olsen, E. T., Fetzer, E., Hulley, G., Manning, E., Blaisdell, J., Iredell, L., Susskind, J., Warner, J., Wei, Z., Blackwell, W., and et al.: AIRS/AMSU/HSB version 6 level 2 product user guide, NASA-JPL Tech. Rep., p. 134, 2013.
- 10 Pan, L. L., Honomichl, S. B., Kinnison, D. E., Abalos, M., Randel, W. J., Bergman, J. W., and Bian, J. C.: Transport of chemical tracers from the boundary layer to stratosphere associated with the dynamics of the Asian summer monsoon, *J. Geophys. Res. Atmos.*, 121, 14,159–14,174, <https://doi.org/10.1002/2016JD025616>, 2016.
- Park, M., Randel, W. J., Emmons, L. K., and Livesey, N. J.: Transport pathways of carbon monoxide in the Asian summer monsoon diagnosed from Model of Ozone and Related Tracers (MOZART), *J. Geophys. Res.*, 114, D08303, <https://doi.org/10.1029/2008JD010621>, 2009.
- 15 Ploeger, F., Konopka, P., Günther, G., Grooß, J.-U., and Müller, R.: Impact of the vertical velocity scheme on modeling transport across the tropical tropopause layer, *J. Geophys. Res.*, 115, D03301, <https://doi.org/10.1029/2009JD012023>, 2010.
- Ploeger, F., Gottschling, C., Griebbach, S., Grooß, J.-U., Günther, G., Konopka, P., Müller, R., Riese, M., Stroh, F., Tao, M., Ungermann, J., Vogel, B., and von Hobe, M.: A potential vorticity-based determination of the transport barrier in the Asian summer monsoon anticyclone, *Atmos. Chem. Phys.*, 15, 13 145–13 159, <https://doi.org/10.5194/acp-15-13145-2015>, 2015.
- 20 Pommrich, R., Müller, R., Grooß, J.-U., Konopka, P., Ploeger, F., Vogel, B., Tao, M., Hoppe, C. M., Günther, G., Spelten, N., Hoffmann, L., Pumphrey, H.-C., Viciani, S., D’Amato, F., Volk, C. M., Hoor, P., Schlager, H., and Riese, M.: Tropical troposphere to stratosphere transport of carbon monoxide and long-lived trace species in the Chemical Lagrangian Model of the Stratosphere (CLaMS), *Geosci. Model Dev.*, 7, 2895–2916, <https://doi.org/10.5194/gmd-7-2895-2014>, 2014.
- Randel, W. J., Park, M., Emmons, L., Kinnison, D., Bernath, P., Walker, K. A., Boone, C., and Pumphrey, H.: Asian Monsoon Transport of
25 Pollution to the Stratosphere, *Science*, 328, 611–613, <https://doi.org/10.1126/science.1182274>, 2010.
- Rosen, J. M. and Kjöme, N. T.: Backscattersonde: a new instrument for atmospheric aerosol research, *Appl. Opt.*, 30, 1552–1561, <https://doi.org/10.1029/97JD01486>, 1991.
- Song, Y., Lü, D., Li, Q., Bian, J., Wu, X., and Li, D.: The impact of cut-off lows on ozone in the upper troposphere and lower stratosphere over Changchun from ozonesonde observations, *Adv. Atmos. Sci.*, 33, 135–150, <https://doi.org/10.1007/s00376-015-5054-2>, 2016.
- 30 Stevenson, D. S., Young, P. J., Naik, V., Lamarque, J.-F., Shindell, D. T., Voulgarakis, A., Skeie, R. B., Dalsoren, S. B., Myhre, G., Berntsen, T. K., Folberth, G. A., Rumbold, S. T., Collins, W. J., MacKenzie, I. A., Doherty, R. M., Zeng, G., van Noije, T. P. C., Strunk, A., Bergmann, D., Cameron-Smith, P., Plummer, D. A., Strode, S. A., Horowitz, L., Lee, Y. H., Szopa, S., Sudo, K., Nagashima, T., Josse, B., Cionni, I., Righi, M., Eyring, V., Conley, A., Bowman, K. W., Wild, O., and Archibald, A.: Tropospheric ozone changes, radiative forcing and attribution to emissions in the Atmospheric Chemistry and Climate Model Intercomparison Project (ACCMIP), *Atmos. Chem. Phys.*,
35 13, 3063–3085, <https://doi.org/10.5194/acp-13-3063-2013>, <https://www.atmos-chem-phys.net/13/3063/2013/>, 2013.
- Stohl, A. and Trickl, T.: A textbook example of longrange transport: Simultaneous observation of ozone maxima of stratospheric and North American origin in the free troposphere over Europe, *J. Geophys. Res.*, 104, 30 445–30 462, <https://doi.org/10.1029/1999JD900803>, <http://https://doi.org/10.1029/1999JD900803>, 1999.



- Stohl, A., Bonasoni, P., Cristofanelli, P., Collins, W., Feichter, J., Frank, A., Forster, C., Gerasopoulos, E., Gäggeler, H., James, P., Kentarchos, T., Kromp-Kolb, H., Krüger, B., Land, C., Meloen, J., Papayannis, A., Priller, A., Seibert, P., Sprenger, M., Roelofs, G. J., Scheel, H. E., Schnabel, C., Siegmund, P., Tobler, L., Trickl, T., Wernli, H., Wirth, V., Zanis, P., and Zerefos, C.: Stratosphere-troposphere exchange: A review, and what we have learned from STACCATO, *J. Geophys. Res.*, 108, <https://doi.org/10.1029/2002JD002490>, <https://agupubs.onlinelibrary.wiley.com/doi/abs/10.1029/2002JD002490>, 2003.
- 5 Tissier, A.-S. and Legras, B.: Convective sources of trajectories traversing the tropical tropopause layer, *Atmos. Chem. Phys.*, 16, 3383–3398, <https://doi.org/10.5194/acp-16-3383-2016>, 2016.
- Trickl, T., Feldmann, H., Kanter, H.-J., Scheel, H.-E., Sprenger, M., Stohl, A., and Wernli, H.: Forecasted deep stratospheric intrusions over Central Europe: case studies and climatologies, *Atmos. Chem. Phys.*, 10, 499–524, <https://doi.org/10.5194/acp-10-499-2010>, <https://www.atmos-chem-phys.net/10/499/2010/>, 2010.
- 10 Trickl, T., Vogelmann, H., Giehl, H., Scheel, H.-E., Sprenger, M., and Stohl, A.: How stratospheric are deep stratospheric intrusions?, *Atmos. Chem. Phys.*, 14, 9941–9961, <https://doi.org/10.5194/acp-14-9941-2014>, <https://www.atmos-chem-phys.net/14/9941/2014/>, 2014.
- Vernier, J. P., Fairlie, T. D., Natarajan, M., Wienhold, F. G., Bian, J., Martinsson, B. G., Crumeyrolle, S., Thomason, L. W., and Bedka, K. M.: Increase in upper tropospheric and lower stratospheric aerosol levels and its potential connection with Asian pollution, *J. Geophys. Res. Atmos.*, <https://doi.org/10.1002/2014JD022372>, 2015.
- 15 Vernier, J.-P., Fairlie, T. D., Deshler, T., Ratnam, M. V., Gadhavi, H., Kumar, B. S., Natarajan, M., Pandit, A. K., Raj, S. T. A., Kumar, A. H., Jayaraman, A., Singh, A. K., Rastogi, N., Sinha, P. R., Kumar, S., Tiwari, S., Wegner, T., Baker, N., Vignelles, D., Stenchikov, G., Shevchenko, I., Smith, J., Bedka, K., Kesarkar, A., Singh, V., Bhate, J., Ravikiran, V., Rao, M. D., Ravindrababu, S., Patel, A., Vernier, H., Wienhold, F. G., Liu, H., Knepp, T. N., Thomason, L., Crawford, J., Ziemba, L., Moore, J., Crumeyrolle, S., Williamson, M., Berthet, G., Jégou, F., and Renard, J.-B.: BATAL: The balloon measurement campaigns of the Asian tropopause aerosol layer, *Bull. Amer. Meteor. Soc.*, 99, 955–973, <https://doi.org/10.1175/BAMS-D-17-0014.1>, <https://doi.org/10.1175/BAMS-D-17-0014.1>, 2018.
- 20 Vogel, B., Pan, L. L., Konopka, P., Günther, G., Müller, R., Hall, W., Campos, T., Pollack, I., Weinheimer, A., Wei, J., Atlas, E. L., and Bowman, K. P.: Transport pathways and signatures of mixing in the extratropical tropopause region derived from Lagrangian model simulations, *J. Geophys. Res.*, 116, D05306, <https://doi.org/10.1029/2010JD014876>, 2011.
- 25 Vogel, B., Günther, G., Müller, R., Groß, J.-U., Hoor, P., Krämer, M., Müller, S., Zahn, A., and Riese, M.: Fast transport from Southeast Asia boundary layer sources to northern Europe: rapid uplift in typhoons and eastward eddy shedding of the Asian monsoon anticyclone, *Atmos. Chem. Phys.*, 14, 12 745–12 762, <https://doi.org/10.5194/acp-14-12745-2014>, 2014.
- Vogel, B., Günther, G., Müller, R., Groß, J.-U., and Riese, M.: Impact of different Asian source regions on the composition of the Asian monsoon anticyclone and of the extratropical lowermost stratosphere, *Atmos. Chem. Phys.*, 15, 13 699–13 716, <https://doi.org/10.5194/acp-15-13699-2015>, 2015.
- 30 Vogel, B., Günther, G., Müller, R., Groß, J.-U., Afchine, A., Bozem, H., Hoor, P., Krämer, M., Müller, S., Riese, M., Rolf, C., Spelten, N., Stiller, G. P., Ungermann, J., and Zahn, A.: Long-range transport pathways of tropospheric source gases originating in Asia into the northern lower stratosphere during the Asian monsoon season 2012, *Atmos. Chem. Phys.*, 16, 15 301–15 325, <https://doi.org/10.5194/acp-16-15301-2016>, 2016.
- 35 Vogel, B., Müller, R., Günther, G., Spang, R., Hanumanthu, S., Li, D., Riese, M., and Stiller, G. P.: Lagrangian simulations of the transport of young air masses to the top of the Asian monsoon anticyclone and into the tropical pipe, *Atmos. Chem. Phys. Discuss.*, 2018, 1–38, <https://doi.org/10.5194/acp-2018-724>, <https://www.atmos-chem-phys-discuss.net/acp-2018-724/>, 2018.



- Vömel, H., Naebert, T., Dirksen, R., and Sommer, M.: An update on the uncertainties of water vapor measurements using cryogenic frost point hygrometers, *Atmos. Meas. Tech.*, 9, 3755–3768, <https://doi.org/10.5194/amt-9-3755-2016>, <https://www.atmos-meas-tech.net/9/3755/2016/>, 2016.
- Vömel, H., David, D. E., and Smith, K.: Accuracy of tropospheric and stratospheric water vapor measurements by the cryogenic frost point hygrometer: Instrumental details and observations, *J. Geophys. Res.*, 112, D08305, <https://doi.org/10.1029/2006JD007224>, 2007.
- Škerlak, B., Sprenger, M., and Wernli, H.: A global climatology of stratosphere-troposphere exchange using the ERA-Interim data set from 1979 to 2011, *Atmos. Chem. Phys.*, 14, 913–937, <https://doi.org/10.5194/acp-14-913-2014>, <https://www.atmos-chem-phys.net/14/913/2014/>, 2014.
- Weigel, K., Hoffmann, L., Günther, G., Khosrawi, F., Olschewski, F., Preusse, P., Spang, R., Stroh, F., and Riese, M.: A stratospheric intrusion at the subtropical jet over the Mediterranean Sea: air-borne remote sensing observations and model results, *Atmos. Chem. Phys.*, 12, 8423–8438, <https://doi.org/10.5194/acp-12-8423-2012>, 2012.
- WMO: Definition of the tropopause, *WMO Bull.*, pp. 134–138, 1957.
- Yan, R. C. and Bian, J. C.: Tracing the boundary layer sources of carbon monoxide in the Asian summer monsoon anticyclone using WRF–Chem, *Adv. Atmos. Sci.*, 32, 943–951, <https://doi.org/10.1007/s00376-014-4130-3>, 2015.
- Yang, H., Chen, G., Tang, Q., and Hess, P.: Quantifying isentropic stratosphere-troposphere exchange of ozone, *J. Geophys. Res. Atmos.*, 121, 3372–3387, <https://doi.org/10.1002/2015JD024180>, 2016.
- Yu, P., Rosenlof, K. H., Liu, S., Telg, H., Thornberry, T. D., Rollins, A. W., Portmann, R. W., Bai, Z., Ray, E. A., Duan, Y., Pan, L. L., Toon, O. B., Bian, J., and Gao, R.-S.: Efficient transport of tropospheric aerosol into the stratosphere via the Asian summer monsoon anticyclone, *P. Natl. Acad. Sci.*, 114, 6972–6977, <https://doi.org/10.1073/pnas.1701170114>, <http://www.pnas.org/content/114/27/6972>, 2017.

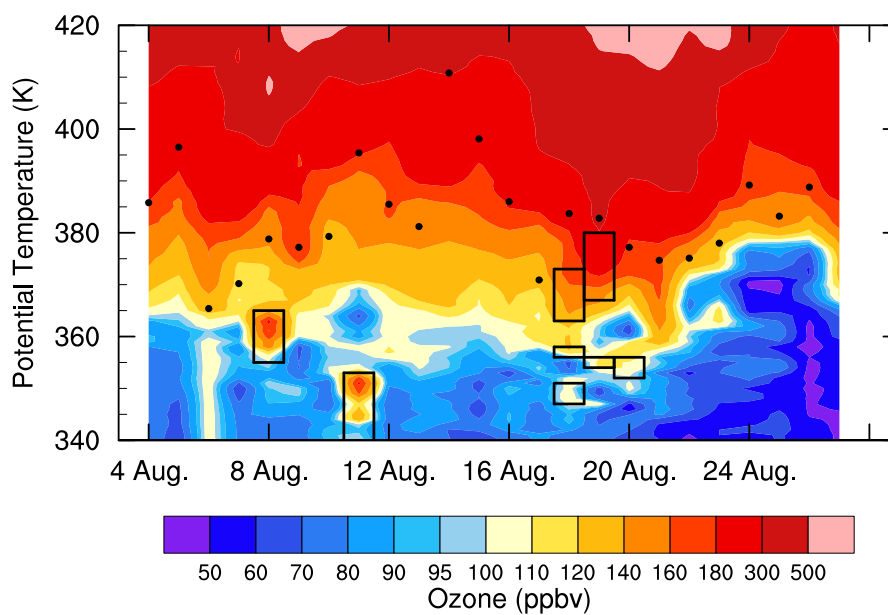


Figure 1. Daily variations of ozone mixing ratios (OMR) between 340 K and 430 K during 4–27 August 2013 from balloon measurements launched in Lhasa. The black dots represent the lapse rate tropopause. High tropospheric ozone is shown by the black rectangle.

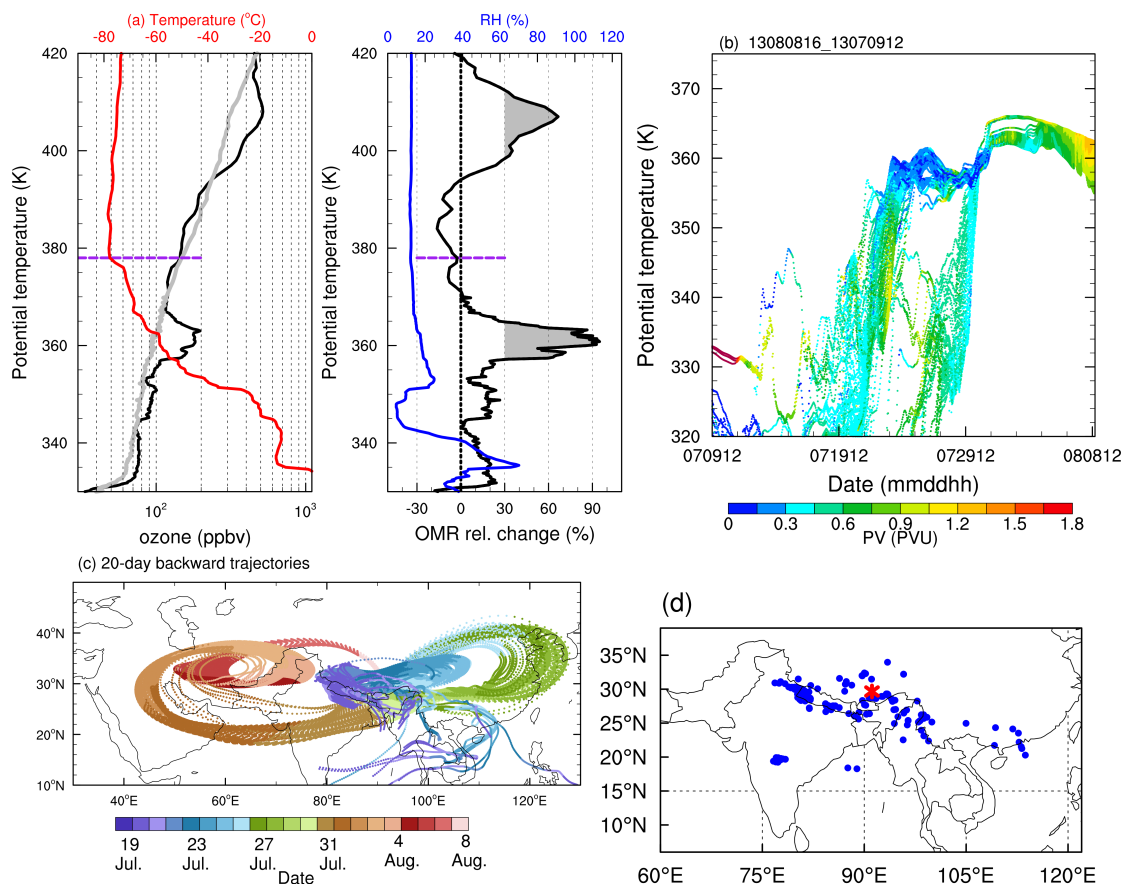


Figure 2. (a) Vertical profiles of ozone (black), monthly mean ozone (grey), and temperature (degree in red), OMR relative change, and relative humidity (blue) in Lhasa on 08 August 2013 at 14:00 UTC. The horizontal line marks the lapse rate tropopause. (b) Potential vorticity ($1 \text{ PVU} = 10^6 \text{ K m}^2 \text{ kg}^{-1} \text{ s}^{-1}$) along the 30-day backward trajectories of air parcels within the high ozone layer (355–362.3 K) as a function of time and potential temperature. (c) 20-day backward trajectories of air parcels between 355 K and 362.3 K at the Lhasa site on 08 August 2013 are shown colour-coded by date. (d) Geolocation of air parcels experienced strong uplift in the positive ozone mixing ratio anomalies. The red asterisk marks the location of Lhasa.

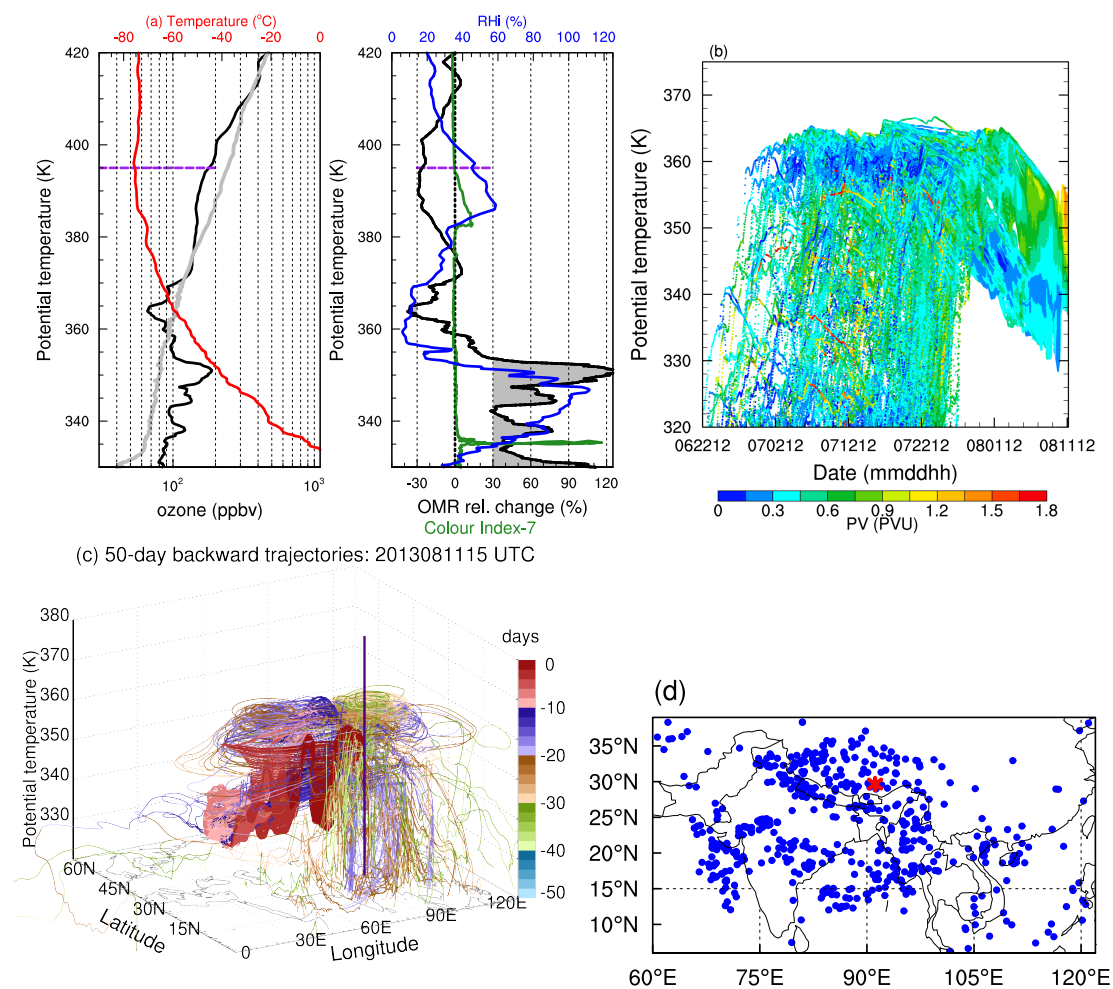


Figure 3. The same as Fig. 2 except for (c) but on 11 August 2013. (a) Clour index (CI) minus 7 ($CI-7 > 0$ marks the cirrus cloud layer, green line). (c) 3-dimensional backward trajectories colour-coded by days.

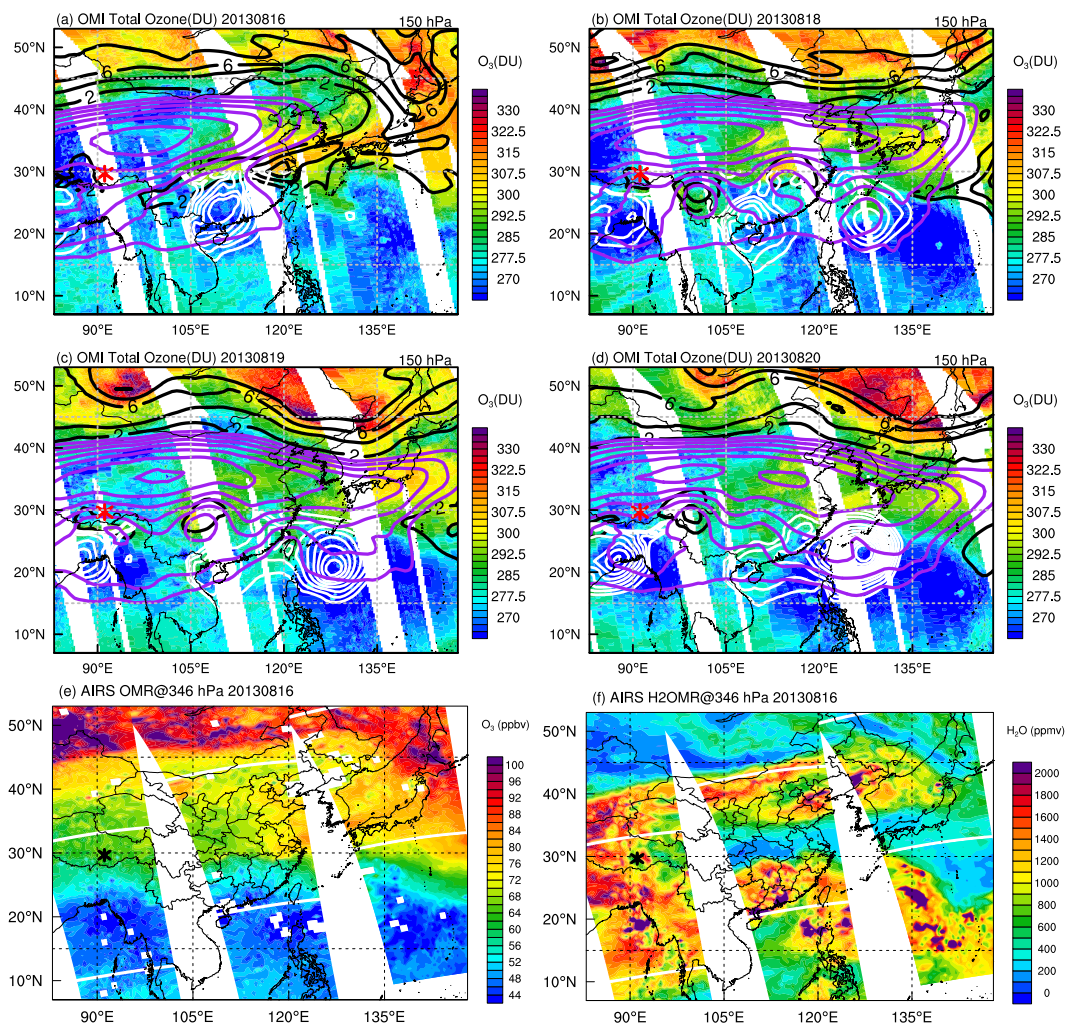


Figure 4. Total column ozone (DU) as measured by OMI with the geopotential height (purple line) and PV (black line, in PVU) at 150 hPa, and the sea-level pressure (white line) of tropical cyclone on (a–d) 16, 18, 19, and 20 August 2013 using ERA-Interim data. (e) Ozone and (f) water vapour mixing ratios for 346 hPa from AIRS on 16 August 2013. The asterisk marks the location of Lhasa.

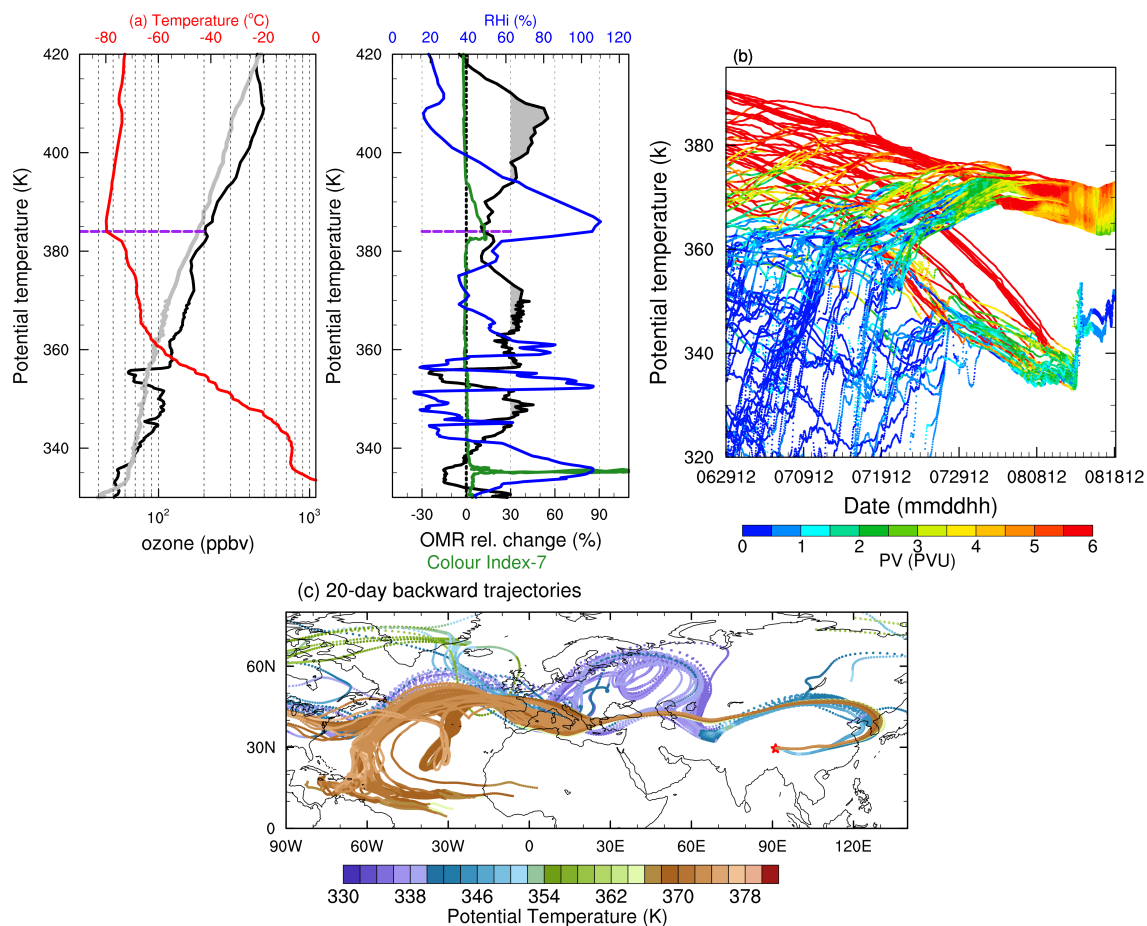


Figure 5. Panels (a, b) are the same as Fig. 3a–b but on 18 August 2013. (c) 20-day backward trajectories of air parcels within high ozone layer are shown colour-coded by potential temperature.

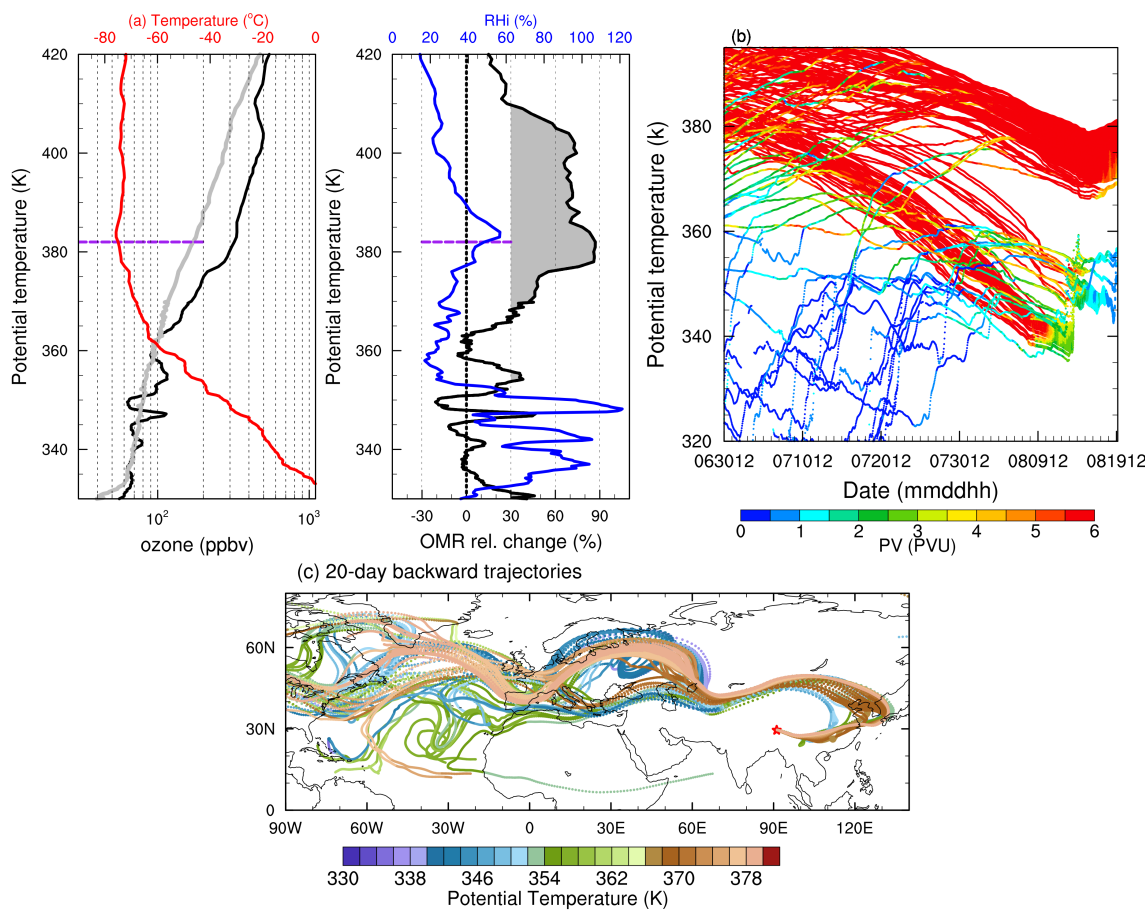


Figure 6. The same as Fig. 5, but on 19 August 2013.

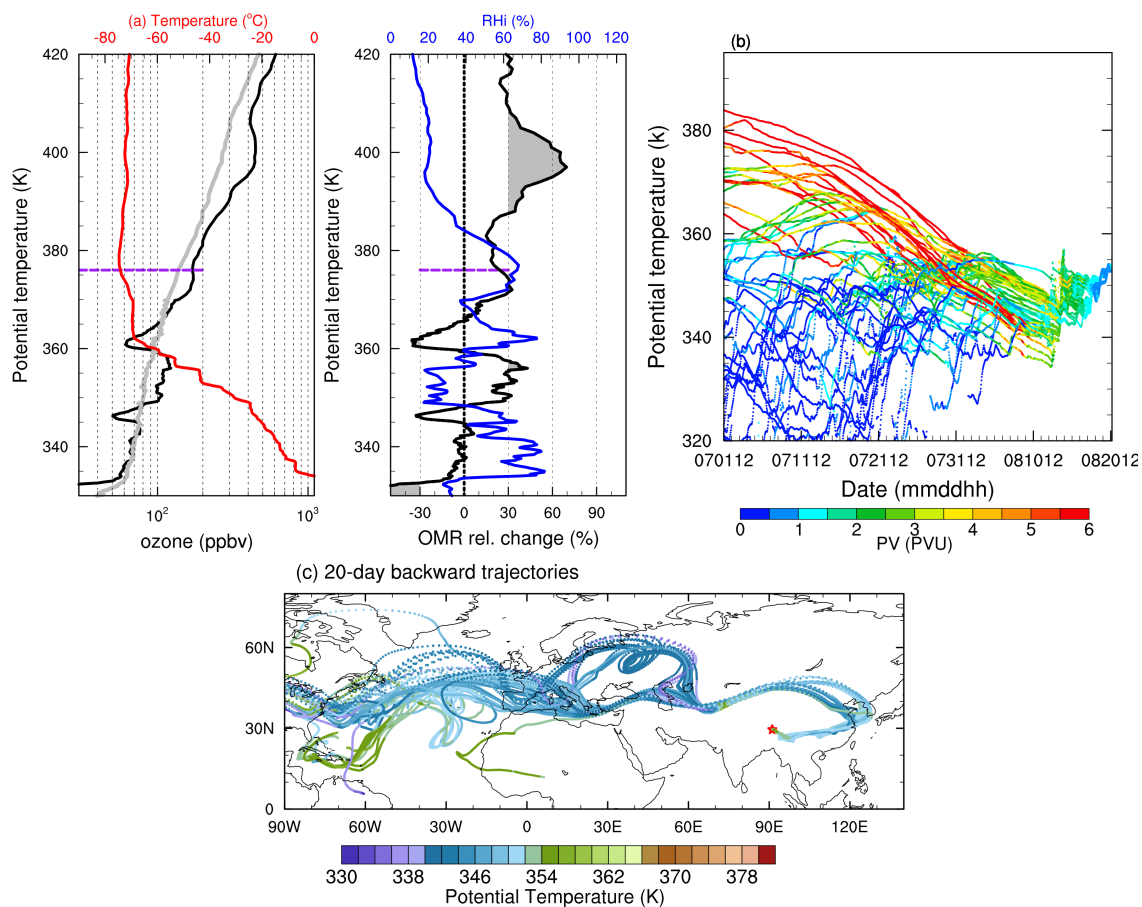


Figure 7. The same as Fig. 5, but on 20 August 2013.

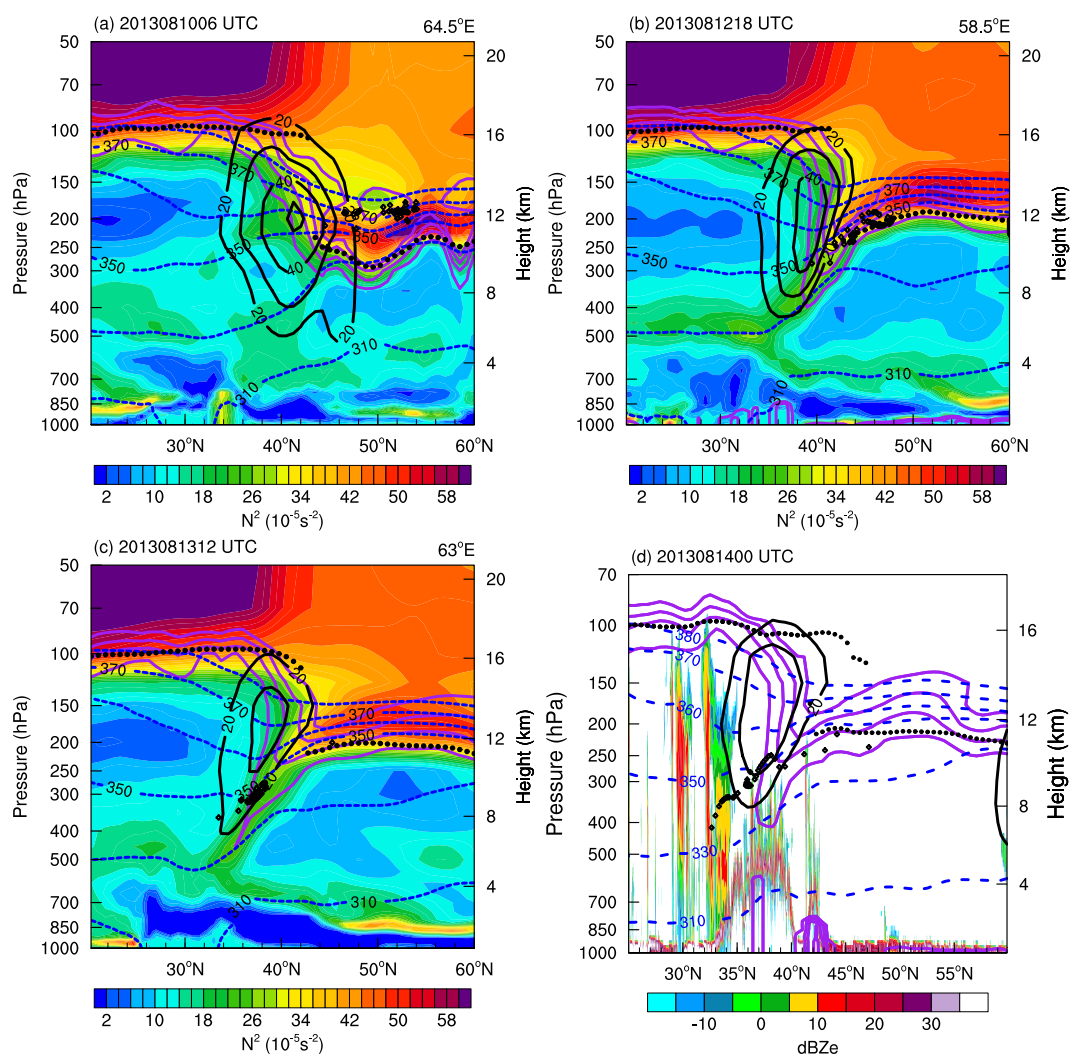


Figure 8. Latitude–pressure cross section of the square of the Brunt–Vaisala frequency (N^2) along the average longitude of the bottom air parcels in Fig. 5b on (a) 10 August at 06:00 UTC, (b) 12 August at 18:00 UTC, (c) 13 August at 12:00 UTC with potential temperature (blue dashed lines, K), PV (purple lines, PVU), tropopause (black dots, hPa), zonal wind (black lines), and air parcels (diamonds). (d) The same as Figure 6a except for radar reflectivity (dBZe) but on 14 August at 00:00 UTC.